

Crystallisation kinetics of supercooled liquid palladium

Zuzanna Kostera *

0009-0002-4729-5523

Warsaw University of Technology Faculty of Physics Koszykowa 75 Warsaw PL

zuzanna.kostera.dokt@pw.edu.pl

Christian Bressler

0000-0001-9694-5495

European XFEL Holzkoppel 4 22869 Schenefeld DE University of Hamburg Department of Physics Luruper

Chaussee 149, 22761 Hamburg DE The Hamburg Centre for Ultrafast Imaging Luruper Chaussee 149,

22761 Hamburg DE

Przemysław Dziegielewski

0000-0002-7544-3960

Warsaw University of Technology Faculty of Physics Warsaw PL

przemyslaw.dziegielewski@pw.edu.pl

Wojciech Gawelda

0000-0001-7824-9197

Universidad Autonoma de Madrid Department of Chemistry Ciudad Universitaria de Cantoblanco 28049

Madrid ES IMDEA Nanociencia Calle Faraday 9, 28049 Madrid ES Adam Mickiewicz University Faculty of

Physics Uniwersytetu Poznańskiego 2, 61-614 Poznań PL

Konstantinos Georgarakis

0000-0003-0918-7310

Cranfield University School of Aerospace, Transport and Manufacturing Cranfield, MK43 0AL GB

Dmitry Khakhulin

0000-0002-4453-1204

European XFEL Holzkoppel 4 22869 Schenefeld DE

Oleksii I. Liubchenko

0000-0002-9773-0661

Institute of Physics of the Polish Academy of Sciences al. Lotników 32/46 Warsaw PL

Adam Olczak

0000-0002-2933-7884

Warsaw University of Technology Faculty of Physics Koszykowa 75 Warsaw PL

Angel Rodríguez-Fernández

European XFEL Holzkoppel 4 22869 Schenefeld DE

Ryszard Sobierajski

0000-0003-2580-6900

Institute of Physics of the Polish Academy of Sciences al. Lotników 32/46 Warsaw PL

Klaus Sokolowski-Tinten

0000-0002-7979-5357

University of Duisburg-Essen DE

Peihao Sun

0000-0002-3608-1557

Dipartimento di Fisica e Astronomia "Galileo Galilei", Università degli Studi di Padova Padova 35131 IT

Robert W.E. van de Kruijs

0000-0002-4738-0819

Industrial Focus Group XUV Optics, MESA+Institute for Nanotechnology, University of Twente

Drienerlolaan 5 7522 NB Enschede NL

Hazem Yousef

0009-0000-7344-2529

European XFEL Holzkoppel 4 22869 Schenefeld DE

Peter Zalden

0000-0002-8530-0576

European XFEL Holzkoppel 4 22869 Schenefeld DE

Jerzy Antonowicz

0000-0002-7781-7540

Warsaw University of Technology Faculty of Physics Koszykowa 75 Warsaw PL

jerzy.antonowicz@pw.edu.pl

Correspondence: * zuzanna.kostera.dokt@pw.edu.pl

Abstract

In this study, we employ classical molecular dynamics (MD) simulations to investigate the crystallisation kinetics of supercooled liquid palladium and relate the results to time-resolved X-ray diffraction measurements on rapidly quenched Pd thin films. Crystal nucleation and growth rates are determined over the temperature range 700–1150 K (0.38–0.65 T_m) by analysing the evolution of the microstructure during the liquid-to-crystal transition. The self-diffusion coefficient of Pd, obtained from the atomic mean-squared displacement, follows Arrhenius behaviour over the investigated temperature range, with an activation energy of 467(6) meV/atom, consistent with available data for supercooled liquid metals. The steady-state homogeneous nucleation rate exhibits a maximum of approximately $4 \times 10^{35} \text{ m}^{-3} \text{ s}^{-1}$ near $0.5 T_m$. Crystal growth occurs at velocities of the order of meters per second, with a temperature dependence consistent with diffusion-limited Wilson–Frenkel kinetics rather than the collision-limited regime. Based on multiple statistically independent simulations, a time–temperature–transformation (TTT) diagram for crystallisation onset is constructed. The TTT curve exhibits a nose near $0.5 T_m$ and 100 ps, corresponding to a critical cooling rate for vitrification on the order of 10^{13} K/s . The simulations reproduce the crystallisation onset time and temperature observed in time-resolved X-ray diffraction experiments on optically molten Pd thin films quenched at $5 \times 10^{11} \text{ K/s}$. These results indicate that homogeneous, rather than heterogeneous, nucleation governs the achievable supercooling in the experimentally studied films.

Keywords

Crystallisation kinetics, Supercooled liquids, Molecular dynamics simulation, Homogeneous nucleation, Crystal growth, Classical nucleation theory (CNT), XFEL, pump–probe, X-ray diffraction

1. Introduction

Understanding crystallisation in supercooled liquids (SCLs) is a central problem in materials science and condensed-matter physics. The competition between crystallisation and vitrification governs glass formation and sets important processing limits for many materials. Crystallisation in SCLs is controlled by the interplay between thermodynamic driving forces and the kinetics of atomic motion. As the temperature decreases below the equilibrium melting point, the free-energy difference between the liquid and crystalline phases grows, providing an increasingly strong driving force for crystallisation. At the same time, atomic mobility decreases in the progressively more viscous liquid. The balance between these opposing trends ultimately determines whether the liquid crystallises or instead avoids crystallisation and forms an amorphous structure.

SCL metals generally exhibit very low resistance to crystallisation and crystallise almost instantly when quenched below the equilibrium melting point. Only in alloys with a specifically tuned atomic composition, typically near deep eutectics, a high glass-forming ability can be realized. In contrast, pure single-element metals are an extreme case, with exceptionally high nucleation and growth rates of close-packed crystalline phases in the supercooled state [1], [2]. Suppressing crystallisation and thus vitrifying a pure metal is therefore extremely challenging, requiring quenching rates on the order of 10^{14} K/s [3]. The degree of supercooling in metallic liquids can be increased through atomization [4], containerless processing [5], or fluxing treatment [6]. The ultimate stability limit of the SCL is set by homogeneous nucleation, which occurs spontaneously in the bulk and, unlike heterogeneous nucleation, cannot be avoided by removing preferential nucleation sites such as container walls or impurities. This distinction has been questioned in pure metals. In MD simulations of SCL iron, the authors [7] observed small satellite grains near larger ones and new grains nucleating on pre-existing grain surfaces, revealing unexpected complexity in the nucleation process and motivating further studies of SCL crystallisation. After the nucleation stage, crystallisation proceeds via rapid propagation of the solid-liquid interface until another grain is reached. As with nucleation, the mechanism of crystal growth in pure metals remains unresolved, and no comprehensive theory of rapid growth exists [8]. The fundamental question of whether the growth rate is diffusion-limited [9], [10], governed by thermally activated atomic motion, or collision-limited [11], ultimately constrained by the speed of sound in the liquid, remains open [12].

The ultrashort timescales involved in transitions between the liquid and the solid state make direct experimental investigation extremely challenging, so current understanding largely stems from MD simulations [7], [13]–[18]. Early simulations were constrained by

computational resources available at the time, but rapid growth of large-scale MD has since enabled statistically robust measurements of crystallisation kinetics and revealed mesoscale effects, such as non-homogeneous grain distributions [7].

In this work, we utilised MD simulations to study crystal nucleation and growth kinetics in SCL palladium (Pd), an elemental basis for numerous glass-forming metallic alloys. By selecting an optimal system size [19], [20] and performing multiple statistically independent runs, we quantified nucleation and growth rates across a wide temperature range, identifying the mechanisms governing crystallisation.

2. Methods

MD simulations

To accurately represent the crystallisation behaviour of the SCL Pd, an embedded-atom method (EAM) interatomic potential developed specifically for pure Pd was employed in this study [21]. All of the MD simulations were performed using the LAMMPS code [22], [23]. Simulations were conducted in the isothermal-isobaric (NPT) ensemble with three-dimensional periodic boundary conditions in a cubic simulation box, a timestep of 2 fs, and no external pressure applied to the system. Both the temperature and pressure were controlled using the Nose-Hoover thermostat and barostat [24]. This setup preserves the correct NPT statistical ensemble and produces well-controlled temperature and pressure trajectories without the velocity rescaling artefacts.

To determine an appropriate simulation system size, a series of preliminary runs was carried out on systems of varying atom counts. The results revealed a pronounced sensitivity of the behaviour of the crystallisation dynamics to system size. Increasing the system size progressively reduced the run-to-run variance in the crystallisation onset time observed in smaller systems. Eventually, a system containing 1,372,000 atoms was selected for the primary simulations, as it yielded consistent, reproducible crystallisation behaviour across independent simulation seeds (different initial coordination structures). Representative results of those preliminary tests are provided in the Supplementary Materials. Moreover, to construct the Time-Temperature-Transformation (TTT) diagram (see the Results section), a complementary series of simulations was performed using a reduced system size of 256,000 atoms. Although individual runs at this size exhibit larger run-to-run variability than those performed on 1,372,000 atoms, the statistical robustness required for the TTT diagram was instead obtained through ensemble averaging. Ten statistically independent simulations were performed at each investigated temperature, and the crystallisation onset time was extracted from their combined distribution. This approach trades single-run

reproducibility for ensemble-level statistics, allowing meaningful sampling of nucleation times at each temperature, while keeping the total computational cost tractable.

To investigate the crystallisation process of the SCL, an initial face-centred cubic (FCC) crystalline configuration was first melted and then equilibrated for 100-200 ps at 2500 K, well above the equilibrium melting point of Pd ($T_m = 1828$ K). This step ensured the complete elimination of any residual crystalline order and the erasure of the system's thermal history. The molten Pd system was then instantaneously quenched by setting the target temperature in the range of $0.38T_m$ to $0.65T_m$ and relaxed at that temperature for approximately 3 ns. Following the step change in temperature, the Nose-Hoover thermostat required on average ~ 20 ps to stabilize the system temperature to the set value. This thermalisation interval was excluded from the subsequent analysis of nucleation and growth kinetics, for which the origin of time was reset to the end of the stabilisation period.

We visualised and analysed the growth of crystalline structures in SCL Pd, using OVITO [25] software. Nucleation and growth of crystalline grains (here understood as distinct domains of a system in which the atomic lattice has a uniform orientation) were quantified using OVITO's built-in post-processing tools that apply specific structural analysis algorithms to atomistic simulation data. In particular, Polyhedral Template Matching (PTM) [26] was used in conjunction with the Grain Segmentation algorithm. The PTM algorithm distinguishes between ordered and disordered atomic arrangements and classifies order structures according to their crystallographic structure type (e.g. FCC, BCC, HCP). Subsequently, atoms identified as "disordered" by the PTM algorithm, and therefore not belonging to any grain, were removed from the simulation box before applying the Grain Segmentation. The Grain Segmentation, based on the Grain Clustering algorithm, was applied with a minimum grain size arbitrarily set to 100 atoms. This threshold prevented the algorithm from erroneously assigning small disordered regions or noise-like crystalline fragments as separate grains, thereby allowing more reliable observation of individual grain growth. This combined approach enabled detailed, time-resolved observation of grain evolution and the formation of crystal nuclei at the atomic scale. In particular, it allowed crystallites with different structural orientations to be distinguished. This enabled tracking the growth of individual grains, defined as domains with a continuous crystalline lattice. Such grains could be resolved even within evolving grain clusters that other algorithms may identify as single grains.

XFEL pump-probe experiment

The time-resolved X-ray powder diffraction (XRD) data analysed in this work were acquired at the X-ray Free Electron Laser “European XFEL”, using femtosecond X-ray pulses following sub-ps optical excitation (pump) at 515 nm wavelength. The measurements were conducted on thin polycrystalline Pd films at the Femtosecond X-ray Experiments (FXE) [27] instrument of the European XFEL. The Pd samples consist of a thin polycrystalline Pd film sandwiched between amorphous cap and substrate layers, the full structural and optical characterisation of which is given in ref. [21]. Because the Pd film thickness is comparable to the optical penetration depth of the pump laser, the absorbed energy is deposited nearly uniformly across the film, producing rapid and homogeneous melting. The cap and substrate then act as a large thermal reservoir, into which heat is dissipated by phonon thermal conduction, yielding the cooling rates of the order of 5×10^{11} K/s relevant to the present work. Full details of the experimental setup, measurement protocol, thin-film Pd samples and XRD data processing are provided elsewhere [21]. While the experimental results presented in ref. [21] are limited to short pump-probe delay times (up to 30 ps after the optical excitation), covering the initial melting dynamics, the present work includes long-delay-time data corresponding to the quenching stage. By monitoring the transient XRD patterns of the molten film acquired during the quench, in particular the FWHM of the first liquid structure peak, which depends on temperature, and comparing them with XRD patterns calculated for MD snapshots of the liquid (see Supplementary Material for details), we were able to estimate the film temperature and track the time of crystallisation onset.

3. Results

Our simulation procedure, described in the Methods section, was conducted in the temperature range of $0.38-0.65T_m$, yielding a substantial dataset that enables reliable quantification of SCL crystallisation kinetics. Figure 1 provides an overview of the simulated microstructural evolution at three representative temperatures (750 K, 950 K, and 1150 K) and four selected moments of simulations (100 ps, 500 ps, 1500 ps, and 2500 ps) where the system was kept at set temperature. For each temperature-time combination, Figure 1 shows the simulation box visualised in OVITO with the Grain Segmentation algorithm applied. Each visualised system state is accompanied by its corresponding calculated diffraction pattern, with all plots sharing a common intensity (vertical) axis. The XRD patterns are included because, unlike the visualisations of the simulation box, they are representative of the bulk of the system. The presented set of MD snapshots and corresponding XRD patterns provides an overview of the structural evolution from the SCL to the crystalline state, thereby capturing the kinetics of the crystallisation process.

Judging from the volume density of crystalline grains at 100 ps, the nucleation rate is highest at the intermediate temperature of 950 K. Notably, although the onset of nucleation is clearly visible in the MD snapshots, the low crystalline volume fraction prevents its detection in the calculated XRD patterns, as the diffraction pattern of the liquid does not exhibit distinctive Bragg peaks. A rough analysis of the visualisations reveals that the final (2500 ps) grain structure at 1150 K is significantly coarser than that observed at lower temperatures. This difference is also reflected in the width of the Bragg peaks in the corresponding diffraction patterns, with sharper peaks indicating a larger mean grain size. The differences in the final microstructure are further reflected in the fraction of atoms in a structurally disordered environment, which scales with the grain-boundary contribution. This fraction is approximately 20% for the system crystallising at 1150 K, but increases to about 45% at 750 K (see Supplementary Material).

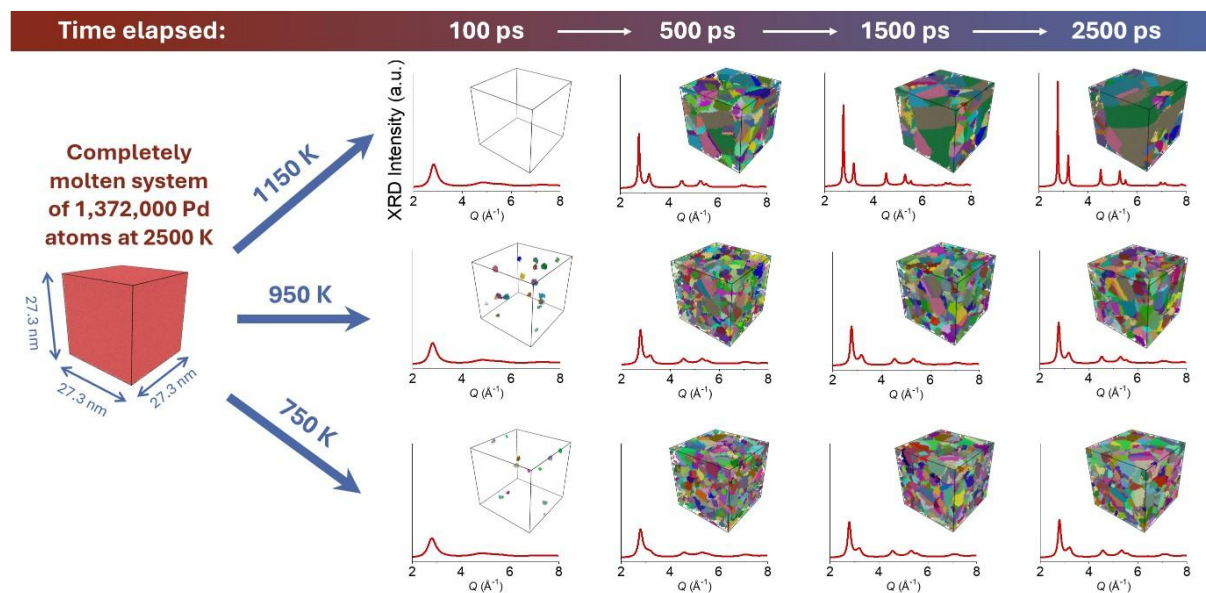


Figure 1: Selected snapshots of the crystalline microstructure and the corresponding diffraction patterns during the structural evolution of the investigated system of 1,372,000 Pd atoms annealed at 750 K, 950 K, and 1150 K. Grain orientations are colour-coded. For clarity, atoms with a disordered environment were omitted from the visualisation.

The snapshots shown in Fig. 1 reflect the underlying crystallisation kinetics, namely the temperature dependence of the rates of crystal nucleation $J(T)$ and growth rate $U(T)$. These dependencies arise from the competition between thermodynamic and kinetic factors in the SCL temperature regime. For both crystal nucleation and growth, increasing supercooling enhances the thermodynamic driving force (i.e. the free-energy difference between the liquid and the crystal) but reduces atomic diffusivity. Since sluggish diffusivity is

the ultimate factor enabling deep supercooling of a liquid, our first step towards revealing the microscopic mechanism of crystallisation was to quantify atomic mobility from MD structural trajectories. To determine the self-diffusion coefficient D of Pd in the liquid, we tracked the mean-squared atomic displacement (MSD) and used the relation [13], [28], [29]:

$$D = \frac{1}{2d} \lim_{t \rightarrow \infty} \frac{\partial \text{MSD}}{\partial t}, \quad (1)$$

where t denotes time and d is the number of spatial dimensions (3 in the present case). The insert in Figure 2 presents the $\text{MSD}(t)$ dependence for a selected temperature of 920 K. This temperature was selected as a representative case for the detailed analysis of crystallisation kinetics because it corresponds to the simulated state closest to $0.5 T_m$ and lies in the vicinity of the nose of the TTT diagram discussed later in this section. After the initial transient of approximately 20 ps, during which atomic motion is inertial and follows a ballistic regime, the MSD begins to exhibit a linear dependence on time, indicating the onset of diffusive behaviour. Since the analysis focuses specifically on liquid-state diffusion, the time window of interest was defined as the interval between the end of the ballistic regime and the onset of crystallisation, which occurred at approximately 120 ps. From the slope of the MSD in this time window, the value of $D \approx 1.6 \times 10^{-10} \text{ m}^2\text{s}^{-1}$ was extracted. As soon as the crystalline phase becomes predominant, the slope of the $\text{MSD}(t)$ curve decreases significantly, since atomic diffusion in the solid is substantially slower than in the liquid. The protocol described above for identifying the appropriate time window for liquid-state diffusion and determining the slope of the $\text{MSD}(t)$ curve was applied at each investigated temperature, yielding the liquid-state diffusion coefficient D as a function of temperature. The results are presented as an Arrhenius plot shown in Figure 2. The linear character of the plot indicates that over the investigated temperature range, D follows an Arrhenius relation

$$D = D_0 \exp\left(-\frac{E_a}{k_B T}\right), \quad (2)$$

where E_a is the activation energy, D_0 is the pre-exponential factor, and k_B is the Boltzmann constant. From the linear fit of $\ln(D)$ vs $1000/T$ parameters, E_a and D_0 , were estimated to be approximately 467(6) meV/atom (or 45.1(6) kJ/mol) and $5.8(4) \times 10^{-8} \text{ m}^2\text{s}^{-1}$, respectively. We note that the slight deviation from linearity in the Arrhenius plot at the lowest temperatures, consistent with a decrease in the activation energy, is accompanied by an increase in the error bars related to the uncertainty in determining the slope of $\text{MSD}(t)$. In our interpretation, this deviation should therefore be considered a numerical artefact.

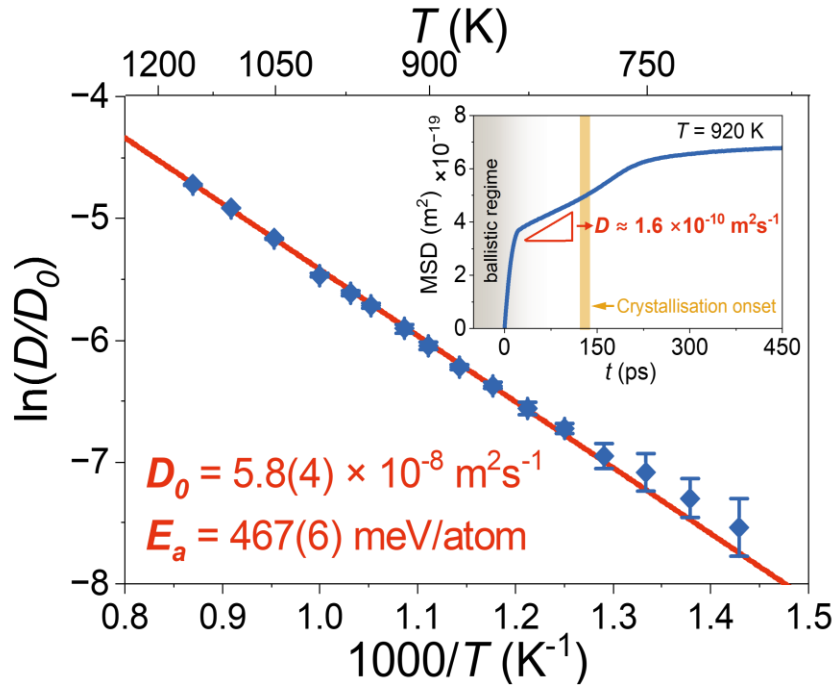


Figure 2: The Arrhenius plot for the liquid self-diffusion coefficient (symbols) and a linear fit (solid line) with E_a and D_0 values. The inset shows the temporal evolution of the MSD at 920 K. The ballistic regime extends over the initial 20 ps, while crystallisation begins at approximately 120 ps. The diffusion coefficient is determined from the slope within this time window.

In the subsequent stage of the analysis, the crystal nucleation and growth rates were determined. The analysis protocol employed in the present work provides, for each analysed simulation timestep, the total number of crystalline grains present in the simulation box whose size exceeds the prescribed minimum-size threshold, together with the number of atoms comprising each individual grain. It should be noted that the application of such a threshold necessarily precludes direct tracking of the earliest stages of crystalline cluster formation and therefore shifts the apparent nucleation onset towards later times. Nevertheless, this procedure substantially reduces the likelihood of erroneously identifying transient crystalline fluctuations, small ordered clusters, or noise-like structural features as stable grains and thus makes the subsequent analysis more reliable. Furthermore, as demonstrated in the following part of this section, the adopted threshold value of 100 atoms is considerably larger than the estimated critical nucleus size throughout the investigated temperature range. Consequently, the applied protocol restricts the analysis to post-critical nuclei, which are expected to be thermodynamically stable with respect to further growth. In the remainder of this work, such post-critical nuclei are therefore referred to as grains.

In what follows, the term “growth rate” refers exclusively to the velocity of the crystal propagation front, measured in the time window between the nucleation stage and the

onset of grain impingement and subsequent coarsening. Correct identification of the coarsening stage onset is therefore an essential step of the MD snapshot analysis. Beyond this point, the evolution of the average grain size is no longer controlled by the motion of the liquid-solid interface, but by the reduction of the total grain-boundary surface area, i.e. the minimisation of the total energy of the system. Since polymorphic crystallisation of a monoatomic metal is a purely interface-controlled process [30], limited by the atomic attachment kinetics at the interface rather than by long-range diffusion, the average crystal radius is expected to increase linearly with time, with the slope corresponding to the growth rate. For each grain identified in the simulation, an equivalent spherical radius was computed from the number of atoms it contains. Figure 3b shows the resulting average grain radius as a function of time at $T = 920$ K, corresponding to the data shown in the insert in Fig. 2. The solid line is a linear fit over the interval $110 \text{ ps} < t < 200 \text{ ps}$, and yields an estimated growth rate of 2 m/s .

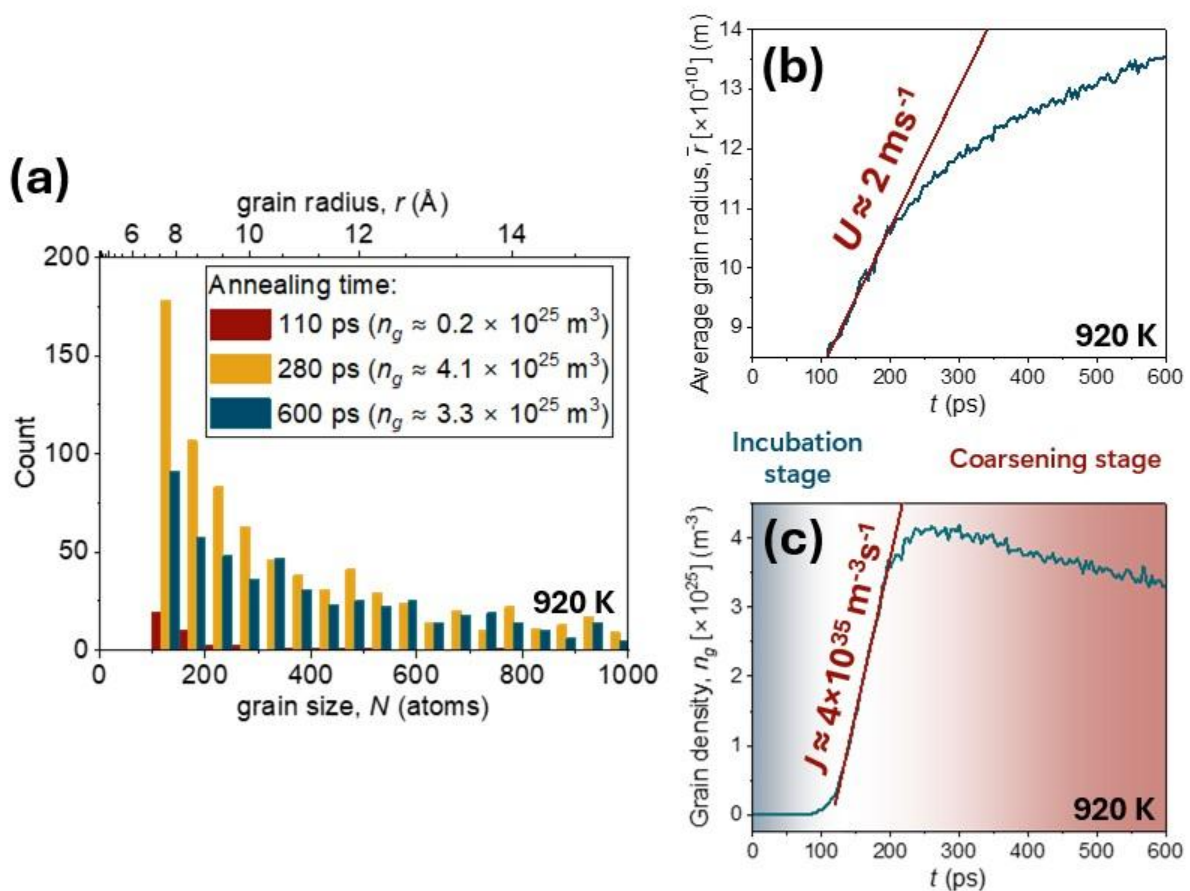


Figure 3: (a) Histograms of grain sizes N at three different moments (110 ps, 280 ps, 600 ps) of annealing of the system at $T = 920$ K, with the upper axis of approximated grain radius (r) corresponding to the grain size. In the legend attached to each histogram, the grain density (n_g) has been indicated. (b) Temporal evolution of the average effective grain radius at 920 K. The red solid line represents the linear best fit, with the slope representing the crystal

growth rate. (c) Temporal evolution of the grain density at 920 K during the first 600 ps. The incubation and grain coarsening stages are indicated by a coloured background with annotations above the plot. The unshaded region corresponds to steady-state nucleation, where the grain density increases linearly with time. The solid line represents the best-fit line, with the slope indicating the steady-state nucleation rate.

The nucleation rate can be readily determined from the temporal evolution of the number density of grains identified by the algorithm. Corresponding grain density (n_g) results are shown in Fig. 3c, complementing the grain size data presented in a histogram in Fig. 3a. The dependence exhibits three distinct temporal regimes: an incubation period during which the grain density remains zero, a regime of linear increase corresponding to steady-state nucleation ($4 \times 10^{35} \text{ m}^{-3} \text{ s}^{-1}$), and a slow decline consistent with grain coarsening. Notably, the onset of coarsening inferred from the grain radius data in Fig. 3b (approximately 200 ps) coincides with the upper temporal limit of the linear increase in grain density observed in Fig. 3c, providing additional support for this interpretation.

The procedure described above for 920 K was applied to all investigated temperatures, yielding the temperature dependence of the nucleation and growth rates. Figure 4a presents the derived nucleation rates over the entire investigated temperature range. The nucleation rate exhibits non-monotonic behaviour, reaching a maximum of $4 \times 10^{35} \text{ m}^{-3} \text{ s}^{-1}$ at the reduced temperature $T/T_m = 0.5$. To extract relevant information on the crystal nucleation mechanisms, we interpreted the MD simulation results within the framework of CNT [2], incorporating the present atomic diffusion data. In CNT, atomic diffusion is incorporated through the kinetic prefactor of the nucleation rate, as the formation and growth of a critical nucleus require atoms to diffuse in the liquid and attach to the crystal interface. The crystal nucleation rate can thus be expressed as

$$J = J_0 \left[\exp\left(-\frac{\Delta G^*}{k_B T}\right) \exp\left(-\frac{E_a}{k_B T}\right) \right], \quad (3)$$

where J_0 is the pre-exponential factor and ΔG^* is the free energy barrier for nucleation separating the metastable liquid from the stable crystal. By fitting the MD-derived $J(T)$ data points to the above described model and using the previously obtained value of $E_a = 45.1(6)$ kJ/mol, we determined a kinetic prefactor $J_0 = 2.3(7) \times 10^{41} \text{ m}^{-3} \text{ s}^{-1}$. Using the enthalpy of fusion, $\Delta H_f = 17.34(73)$ kJ/mol [31], the liquid–crystal surface energy was estimated as $\gamma \approx 0.17(1) \text{ J/m}^2$. Assuming a linear dependence of the thermodynamic driving force for crystallisation ΔG_v on supercooling, $\Delta G_v = \Delta H_f(T_m - T)/T_m$ [2], we calculated the radius of critical nuclei $r^* = 2\gamma/|\Delta G_v|$. The solid line in Fig. 4a represents the resulting $J(T)$ dependence, while Fig. 4b shows the temperature dependence of the critical nucleus radius r^* and the corresponding number of atoms in a critical nucleus. The observed values fall

below the arbitrarily selected threshold of 100 atoms, indicating that our algorithm identifies only supercritical grains. More details of the CNT modelling of the simulated nucleation rate are provided in the Supplementary Material.

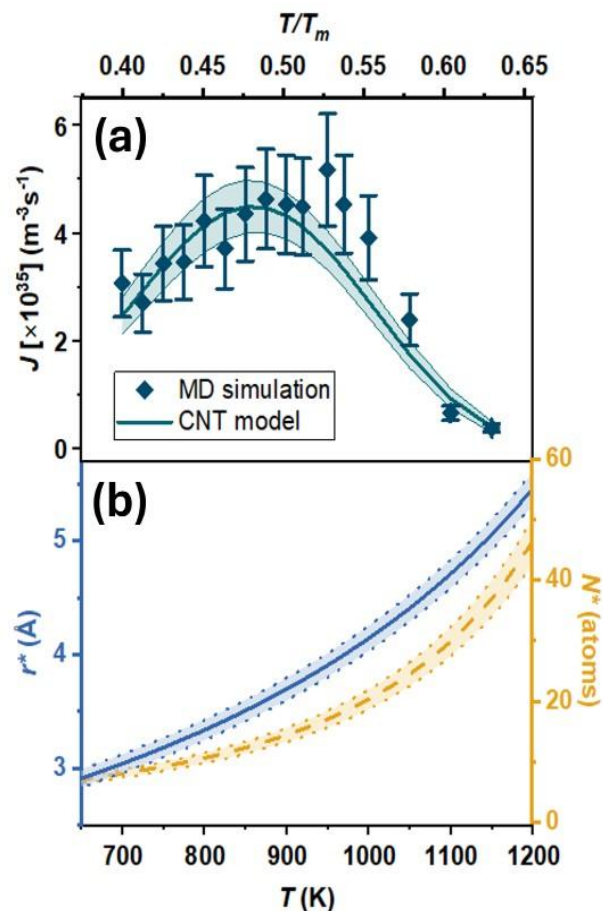


Figure 4: (a) Temperature-dependent crystal nucleation rates obtained from the MD simulation (symbols) with a fitted CNT model (line). (b) The CNT-derived critical nucleus radius r^* (solid line) compared with the CNT-derived critical nucleus size N^* (dashed line) for the values corresponding to the investigated temperature range.

Figure 5 plots the crystal growth rate as a function of annealing temperature. Unlike the nucleation rate, the growth rate increases monotonically with temperature, from approximately 1 m/s to 8 m/s over the studied range, with the rate of increase becoming progressively smaller at higher temperatures.

To interpret this behaviour, the MD data were compared with diffusion-limited and collision-limited growth models. First, the simulation results were fitted with the diffusion-limited Wilson–Frenkel expression [9], [10]:

$$U = f \cdot a \cdot v \cdot \exp\left(-\frac{E_a}{k_B T}\right) \cdot \left(1 - \exp\left(-\frac{\Delta G_v}{k_B T}\right)\right), \quad (4)$$

where f is the density of growth sites, a is a distance the interface advances when a “liquid” atom manages to attach itself to the crystal, and ν is a frequency of the order of the Debye frequency. Approximating a by the atomic size of Pd ($a \approx 2.72 \text{ \AA}$) and using the expression $\nu_D = \frac{k_B \theta_D}{h}$ (with $\theta_D = 274 \text{ K}$ for Pd [32]) to evaluate ν ($\sim 5.71 \text{ THz}$), the best fit is obtained for $f = 0.67$. The parameter f is a dimensionless factor accounting for the efficiency of atomic attachment at the liquid-crystal interface. The present value of approximately 2/3 suggests the existence of a rough solid–liquid interface. As shown in the Fig. 5, the realistic parameter set for the diffusion-limited growth model yields a good fit to both the temperature dependence and the magnitude of the growth rate. The same prefactor combination was then used to evaluate U within the collision-limited growth model [33]:

$$U = f \cdot \frac{a}{\lambda} \cdot \sqrt{\frac{3k_B T}{m}} \cdot \left(1 - \exp\left(-\frac{\Delta G_v}{k_B T}\right)\right), \quad (5)$$

where λ is the travel distance of atoms moving at thermal velocity $\sqrt{\frac{3k_B T}{m}}$, and m is the atomic mass. In the general case, λ is a fraction of a , and thus $\lambda = a$ represents a lower limit for the collision-limited growth rate. The yellow dashed line in Fig. 5 represents the prediction for the collision-limited growth under the assumption of $\lambda \approx a$ and $f = 0.67$, deduced from Eq. 5. The resulting values of growth rates corresponding to the collision-limited model span from 150 m/s to 250 m/s across the studied temperature range. These predictions exceed the MD-derived values by nearly two orders of magnitude, indicating that the collision-limited growth model is inadequate for the investigated system.

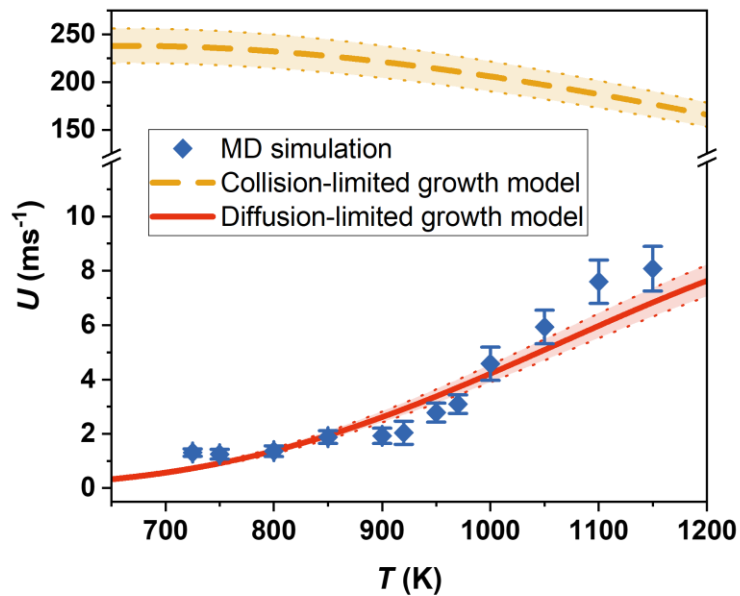


Figure 5: The growth rates determined from the temporal variation of the average effective grain radius (solid symbols) are paired with grain growth rate values derived from the diffusion-limited growth model (solid line) and collision-limited grain growth model (dashed line).

To validate the predictions of our simulations, the MD results were compared with experimental data on the crystallisation of deeply supercooled thin Pd films. The initially polycrystalline films were melted by a single optical laser pulse and, after a tunable delay time, probed by an X-ray pulse, for which the diffraction pattern in transmission geometry was recorded. Since the interaction of the X-ray pulse with the film resulted in permanent damage (although after the structural information was obtained, so-called “probe-before-destroy” approach), each diffraction pattern was collected from a fresh sample spot. The resulting diffraction patterns, representing transient states of the system, were analysed by deconvolution into contributions from the broad liquid peak and the sharp Bragg peaks of the solid fraction [21]. The crystalline and liquid volume fractions, determined from the relative areas of the corresponding peaks, are plotted in the top panel of Fig. 6a as a function of delay time. The bottom panel shows the corresponding film temperature, estimated from the width of the first peak of the liquid structure factor, following the procedure described in the Methods section. As seen in the figure, the first signatures of the liquid phase appear approximately 3 ps after excitation, at the equilibrium melting temperature (1828 K), and melting is complete by 5 ps, as no crystalline signatures remain. The temperature of the molten film continues to increase until about 10 ps, exceeding 2500 K. Next, cooling sets in as energy transfer from the hot electrons to the lattice is completed and heat dissipates into the cap and substrate layers. The liquid persists for approximately

2.5 ns, during which the temperature decreases to about 1200 K, corresponding to an average cooling rate of 5×10^{11} K/s, after which the onset of crystallisation is detected. The dataset presented in Fig. 6 provides an opportunity for a quantitative comparison between the MD-estimated and experimentally measured kinetics of crystallisation of SCL Pd. This comparison can be effectively performed by pinpointing the crystallisation onset on the theoretically predicted TTT diagram shown in Fig. 6b. In this work, the TTT diagram represents the time required for the onset of crystallisation at a given annealing temperature [30]. The resulting C-shaped curve arises from the competition between the thermodynamic driving force and the atomic mobility. The minimum-time point of the curve, known as the “nose”, determines the critical cooling rate for glass formation, since only quenches faster than this rate can avoid the crystallisation region and result in vitrification. In Fig. 6b each point in this diagram represents the temperature and time of crystallisation onset obtained from 10 statistically independent simulation runs involving 256,000 atoms, with error bars indicating the standard deviation of the crystallisation onset times. As shown in the figure, the magnitude of the error bars depends strongly on temperature, reflecting the change in the statistical character of crystallisation across the studied range. At lower temperatures, the nucleation rate is high and many supercritical nuclei form nearly simultaneously within each simulation box. Averaging over a number of nucleation events in a single run effectively smooths the inherently stochastic nature of nucleation, so that the crystallisation onset times are reproducible between independent seeds. At higher temperatures, by contrast, the nucleation rate is low and only a few supercritical nuclei appear in each box. Once formed, they grow rapidly because of the higher atomic mobility, so the onset time is essentially set by the appearance of the first critical nucleus, which is a rare and statistically fluctuating event that varies considerably between seeds. Both regimes correspond to nucleation-limited crystallisation. The difference lies in whether the stochastic nature of nucleation is averaged out within each simulation (low T, many events per run) or only across the ensemble of simulations (high T, few events per run). The dense temperature sampling nevertheless allows the TTT curve to be reliably traced across the entire studied range. The position of the nose (approximately 100 ps at $T/T_m \approx 0.5$) yields a critical cooling rate of 10^{13} K/s for bypassing crystallisation. This cooling rate exceeds that deduced from the experimental data shown in Fig. 6a by more than an order of magnitude, indicating that the experimental cooling rate is insufficient to avoid crystallisation of Pd, consistent with the observations. Furthermore, the time and temperature of the crystallisation onset predicted by the MD simulations fall within the estimated error bars of the experimental data, providing strong support for the validity of the present modelling approach.

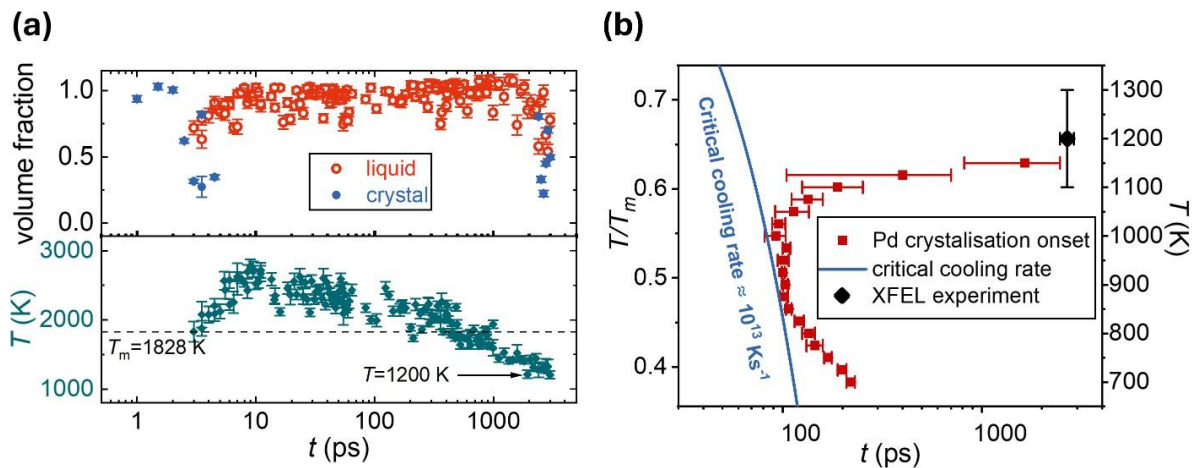


Figure 6: (a) Upper panel presents volume fraction of liquid (open symbols) and crystalline (full symbols) phase observed in diffraction data of thin Pd films in pump-probe XFEL experiment. Bottom panel presents the temporal relation of temperature during the XFEL experiment, estimated using MD simulations; (b) Time-temperature-transformation (TTT) diagram for the crystallisation onset in SCL Pd. Each data point (full squares) represents the average of 10 statistically independent simulation runs involving 256,000 atoms. Error bars indicate the standard deviation of the crystallisation onset times. The solid line marks the critical cooling rate required to bypass crystallisation. The sole black point on the right side of the graph indicates the crystallisation onset observed in the XFEL experiment (see Fig. 6a).

4. Discussion

In the present work, we developed a realistic numerical model of the crystallisation kinetics of supercooled liquid (SCL) Pd, providing insight into the underlying microscopic mechanisms of the liquid-crystal transition. As noted in the Introduction, Pd serves as an elemental basis for numerous glass-forming metallic alloys, which makes its crystallisation behaviour directly relevant to the broader problem of glass formation in metallic systems. At the same time, Pd is chosen as a model system as it is a representative non-magnetic metal with a moderately high melting point and an FCC equilibrium crystal structure without solid–solid phase transitions. According to the available literature (see [12] and references therein), FCC metals are essentially non-glass-forming systems. Although vitrification of pure BCC metals (e.g. Ta, V) has been demonstrated under extreme cooling rates of approximately 10^{14} K/s in nanobridge geometries [3], no comparable result has been reported for pure FCC metals. Significantly, Pd is a primary constituent of numerous metallic glasses, including multicomponent bulk metallic glasses with record-holding critical cooling rates for vitrification below 1 K/s (see, e.g., [34] and [35]). It follows that SCL Pd can be treated as a limiting case of a rapidly crystallising system, i.e. one exhibiting a low free-energy barrier separating the metastable liquid from the equilibrium crystalline state. The height of this barrier, associated with the work of formation of a critical nucleus, can be

increased by alloying [36]–[38] or by reducing the number of heterogeneous nucleation sites by fluxing treatment [6], [35].

The ultimate limit for liquid supercooling is homogeneous crystal nucleation, which cannot be eliminated and can only be bypassed by rapid quenching. MD simulations provide a suitable framework for studying homogeneous nucleation, as they inherently exclude heterogeneous nucleation sites and enable direct analysis of atomistic nucleation mechanisms. Early experiments by Turnbull on the solidification of small metal droplets [39], aimed at suppressing heterogeneous nucleation via liquid atomisation, indicate that Pd can be supercooled to approximately $0.8T_m$ (by over 330 K) before homogeneous nucleation sets in. These droplet experiments were performed under near-equilibrium cooling conditions and are therefore not directly comparable to the present MD results, which are limited to nanosecond timescales. The maximum supercooling achieved under near-equilibrium conditions can be interpreted as the “infinite-time” limit of the TTT curve. While extrapolation from nanoseconds to seconds and longer timescales must be treated with caution, we conclude that the present results are consistent (or at least do not contradict) the near-equilibrium droplet experiments in terms of crystallisation kinetics.

A more relevant comparison between the modelling results and the experiment can be made for rapidly quenched thin films, for which the experimental timescale bridges that of the MD simulations. This overlap in timescales provides a unique opportunity for direct validation of the numerical modelling predictions and, in turn, for a physically meaningful interpretation of the experimental results. This comparison yields good agreement between the experimental findings and theoretical predictions, with the experimentally observed supercooling reaching approximately $T/T_m \approx 0.65$. In terms of interpreting the experimental data, this agreement suggests that rapidly quenched Pd thin films crystallize primarily via homogeneous nucleation and that their supercooling is therefore inevitably limited under the available quenching rates, which are constrained by the thermal properties of the materials involved in the sample (film thickness, heat capacities of the metallic film and substrate/cap layers, and the thermal conductance of their interfaces) [21], [40]. In particular, the experimentally accessible cooling rates remain well below the critical cooling rate required to bypass crystallisation, thereby preventing vitrification and favouring crystallisation of the SCL Pd.

The present comprehensive model of crystallisation kinetics provides insight into the underlying transition mechanisms through the magnitude and temperature dependence of key kinetic factors, namely the diffusion coefficient, nucleation rate, and growth rate. According to Fig. 2, the diffusion coefficient exhibits Arrhenius behaviour over the entire

investigated temperature range. In particular, no signatures of a crossover indicative of a change in atomic dynamics or a liquid–liquid phase transition are observed [41]. Experimental data on diffusion in pure SCL metals are very scarce, as achieving deep supercooling is extremely challenging, and the available data are largely restricted to temperatures close to the equilibrium melting point. To the best of our knowledge, no experimental data on diffusivity for SCL Pd are available. The existing data on Ni (a group 10 element, like Pd) obtained by quasielastic neutron scattering [42] indicate an Arrhenius behaviour of D in the range from approximately 200 K above to more than 200 K below the melting point (down to $0.87 T_m$) with an activation energy of 470 meV/atom and a pre-exponential factor of $7.7 \times 10^{-8} \text{ m}^2/\text{s}$. Both the Arrhenius behaviour of D and the magnitude of E_a and D_0 are in close agreement with the present results (467(6) meV/atom and $5.8(4) \times 10^{-8} \text{ m}^2\text{s}^{-1}$, respectively). We also note that the present values are consistent with self-diffusivity data for pure liquid transition metals obtained in the equilibrium liquid temperature range [43].

The nucleation rates of the order of $10^{35} \text{ m}^{-3}\text{s}^{-1}$ reported in the present study are close to those reported for MD-simulated SCL Al [44]. The estimated liquid-crystal surface energy $\gamma = 0.17(1) \text{ J/m}^2$ falls within the range typically observed for metals [2], [45], [46]. The value reported by Kelton for Pd [2] (0.207 J/m^2) is slightly higher but remains in reasonable agreement with the present estimate. In our derivation of the critical nucleus radius, we assume a linear scaling of the thermodynamic driving force for nucleation with temperature. The underlying assumption is that the difference in specific heat capacity between the liquid and the crystal can be neglected. While this approximation is reasonable for pure metals at small supercoolings, it becomes less accurate at the larger supercoolings considered in the present work, and thus ΔG_v is progressively overestimated at lower temperatures. Since the critical nucleus radius is inversely proportional to ΔG_v , it may therefore be underestimated. The estimated value of r^* for Pd at $0.8T_m$ (see, e.g., [2]) is approximately 1.2 nm, which, considering the limitations discussed above, can be regarded as a reasonable high-temperature extrapolation of the present results.

Our estimate of the crystal growth rate suggests that the crystallisation front propagates into the liquid at velocities well below the speed of sound [47], being the limiting case for the collision-limited growth model. In terms of the temperature dependence, the present results are more consistent with a diffusion-limited mechanism, indicating that thermal activation of atoms is required for their rearrangement at the liquid–crystal interface.

Whether growth in pure liquid metals is a thermally activated (diffusion-limited) process remains one of the long-standing open questions in solidification theory [10]. The present

results indicate that the collision-limited model overestimates the MD-derived growth velocities by nearly two orders of magnitude across the entire studied temperature range and is inconsistent with the MD data regarding the temperature dependence. Simultaneously, the Wilson–Frenkel expression for growth reproduces the MD data, implying the predominance of the diffusion-limited mechanism. We note that the presently estimated growth rates exceed those deduced from the motion of planar interfaces in MD-simulated FCC metals [48] and from experimentally observed dendrite tip velocities in Ni [1]. We argue that the present case differs from these scenarios, as it does not involve isolated interface motion or dendrite growth, but rather the evolution of multiple interacting grains. This distinction is important when comparing with single-interface benchmarks from the literature. Nevertheless, the observed growth velocities are consistent with findings for other pure metals: in the temperature range $0.38\text{--}0.65 T_m$, where atomic diffusivity decreases substantially, the diffusion-limited Wilson–Frenkel model captures the simulated crystal growth kinetics more accurately than the collision-limited model, whose weak temperature dependence leads to a significant overestimation of growth velocities in this regime. The fitted site-density parameter $f = 0.67$ indicates that not all interfacial sites lead to permanent atomic attachment.

5. Conclusions

This work presents a comprehensive MD-based model of crystallisation in supercooled liquid Pd, showing good agreement with time-resolved X-ray diffraction data for rapidly quenched thin Pd films and employing physically realistic parameters. The model indicates that the supercooling of liquid Pd is limited by homogeneous crystal nucleation to approximately 0.65, even under ultrafast quenching conditions of 5×10^{11} K/s. The results further suggest that homogeneous, rather than heterogeneous, nucleation governs the achievable supercooling in the experimentally studied films. Overall, these findings provide a consistent framework for interpreting and predicting crystallisation behaviour in supercooled metallic systems under extreme quenching conditions.

Author contributions: CRediT

Zuzanna Kostera: Conceptualization, Investigation, Methodology, Visualisation, Writing – original draft, Writing – review and editing. **Christian Bressler:** Investigation, Funding acquisition. **Przemysław Dzięgielewski:** Conceptualization, Methodology, Supervision. **Wojciech Gawęda:** Investigation. **Konstantinos Georgarakis:** Investigation, Writing – review & editing. **Dmitry Khakhulin:** Investigation. **Oleksii I. Liubchenko:** Visualization. **Adam Olczak:** Conceptualization, Investigation, Data curation, Visualization. **Angel Rodriguez-**

Fernandez: Investigation. **Ryszard Sobierajski:** Conceptualization, Funding acquisition, Project administration, Investigation, Methodology, Supervision, Writing – review & editing. **Klaus Sokolowski-Tinten:** Conceptualization, Funding acquisition, Investigation, Methodology, Supervision, Writing – review & editing. **Peihao Sun:** Data analysis. **Robert W.E. van de Kruijs:** Sample preparation. **Hazem Yousef:** Investigation. **Peter Zalden:** Conceptualization, Investigation, Methodology, Supervision, Writing – original draft, Writing – review & editing. **Jerzy Antonowicz:** Conceptualization, Funding acquisition, Project administration, Investigation, Methodology, Supervision, Visualization, Writing – review & editing.

Funding sources

This work was supported by the National Science Centre, Poland, grant agreement No 2021/43/B/ST5/02480, and the Deutsche Forschungsgemeinschaft (DFG, German Research Foundation) through Project 278162697-SFB 1242.

Acknowledgements

This research was carried out with the support of the Interdisciplinary Centre for Mathematical and Computational Modelling, University of Warsaw (ICM UW), under computation allocations No. G98-1896, G99-2123 and G101-2359.

We acknowledge European XFEL in Schenefeld, Germany, for provision of X-ray free-electron laser beamtime at the Scientific Instrument FXE (Femtosecond X-Ray Experiments) and would like to thank the staff for their assistance. The access to the European XFEL was supported by a grant of the Polish Ministry of Education and Science - decision no. 2022/WK/13.

Declaration of generative AI use

During the preparation of this work, the author(s) used Claude (Anthropic) and ChatGPT in order to improve the language and readability of selected passages of the manuscript. After using this tool, the author(s) reviewed and edited the content as needed and take full responsibility for the content of the published article.

References

- [1] D. M. Herlach, P. Galenko, and D. Holland-Moritz, Eds., “Chapter 6 Crystal growth in undercooled melts,” in *Metastable solids from undercooled melts*, in Pergamon materials series, vol. 10. Pergamon, 2007, pp. 195–280. doi: [https://doi.org/10.1016/S1470-1804\(07\)80030-7](https://doi.org/10.1016/S1470-1804(07)80030-7).

- [2] K. F. Kelton, "Crystal Nucleation in Liquids and Glasses," in *Solid State Physics*, Elsevier, 1991, pp. 75–177. doi: 10.1016/S0081-1947(08)60144-7.
- [3] L. Zhong, J. Wang, H. Sheng, Z. Zhang, and S. X. Mao, "Formation of monatomic metallic glasses through ultrafast liquid quenching," *Nature*, vol. 512, no. 7513, pp. 177–180, Aug. 2014, doi: 10.1038/nature13617.
- [4] D. Turnbull, "Kinetics of Solidification of Supercooled Liquid Mercury Droplets," *The Journal of Chemical Physics*, vol. 20, no. 3, pp. 411–424, Mar. 1952, doi: 10.1063/1.1700435.
- [5] K. Georgarakis *et al.*, "Probing the structure of a liquid metal during vitrification," *Acta Materialia*, vol. 87, pp. 174–186, Apr. 2015, doi: 10.1016/j.actamat.2015.01.005.
- [6] Y. He, R. B. Schwarz, and J. I. Archuleta, "Bulk glass formation in the Pd–Ni–P system," *Applied Physics Letters*, vol. 69, no. 13, pp. 1861–1863, Sept. 1996, doi: 10.1063/1.117458.
- [7] Y. Shibuta, S. Sakane, E. Miyoshi, S. Okita, T. Takaki, and M. Ohno, "Heterogeneity in homogeneous nucleation from billion-atom molecular dynamics simulation of solidification of pure metal," *Nat Commun*, vol. 8, no. 1, p. 10, Apr. 2017, doi: 10.1038/s41467-017-00017-5.
- [8] G. Sun, J. Xu, and P. Harrowell, "The mechanism of the ultrafast crystal growth of pure metals from their melts," *Nature Materials*, vol. 17, no. 10, pp. 881–886, Oct. 2018, doi: 10.1038/s41563-018-0174-6.
- [9] K. A. Jackson, "The Interface Kinetics of Crystal Growth Processes," *Interface Science*, vol. 10, no. 2, pp. 159–169, July 2002, doi: 10.1023/A:1015824230008.
- [10] H. Men, "A joint diffusion/collision model for crystal growth in pure liquid metals," *Nature Communications*, vol. 15, no. 1, p. 5749, July 2024, doi: 10.1038/s41467-024-50182-7.
- [11] S. R. Coriell and D. Turnbull, "Relative roles of heat transport and interface rearrangement rates in the rapid growth of crystals in undercooled melts," *Acta Metallurgica*, vol. 30, no. 12, pp. 2135–2139, Dec. 1982, doi: 10.1016/0001-6160(82)90134-1.
- [12] A. L. Greer, "New horizons for glass formation and stability," *Nature Mater*, vol. 14, no. 6, pp. 542–546, 2015, doi: 10.1038/nmat4292.

- [13] F. F. Chen, H. F. Zhang, F. X. Qin, and Z. Q. Hu, "Molecular dynamics study of atomic transport properties in rapidly cooling liquid copper," *The Journal of Chemical Physics*, vol. 120, no. 4, pp. 1826–1831, Jan. 2004, doi: 10.1063/1.1636452.
- [14] X. Sui, Y. Cheng, N. Zhou, B. Tang, and L. Zhou, "Molecular dynamics simulation of the solidification process of multicrystalline silicon from homogeneous nucleation to grain coarsening," *CrystEngComm*, vol. 20, no. 25, pp. 3569–3580, 2018, doi: 10.1039/C8CE00767E.
- [15] M. Papanikolaou, K. Salonitis, M. Jolly, and M. Frank, "Large-Scale Molecular Dynamics Simulations of Homogeneous Nucleation of Pure Aluminium," *Metals*, vol. 9, no. 11, p. 1217, Nov. 2019, doi: 10.3390/met9111217.
- [16] D. V. Louzguine-Luzgin, M. Miyama, K. Nishio, A. A. Tsarkov, and A. L. Greer, "Vitrification and nanocrystallization of pure liquid Ni studied using molecular-dynamics simulation," *The Journal of Chemical Physics*, vol. 151, no. 12, p. 124502, Sept. 2019, doi: 10.1063/1.5119307.
- [17] D. V. Louzguine-Luzgin and A. I. Bazlov, "Crystallization of FCC and BCC Liquid Metals Studied by Molecular Dynamics Simulation," *Metals*, vol. 10, no. 11, p. 1532, Nov. 2020, doi: 10.3390/met10111532.
- [18] A. Olczak *et al.*, "Atomic dynamics and local structural disorder during ultrafast melting of polycrystalline Pd," *Scripta Materialia*, vol. 267, p. 116826, Oct. 2025, doi: 10.1016/j.scriptamat.2025.116826.
- [19] A. Mahata and M. Asle Zaeem, "Size effect in molecular dynamics simulation of nucleation process during solidification of pure metals: Investigating modified embedded atom method interatomic potentials," *Modelling and Simulation in Materials Science and Engineering*, vol. 27, no. 8, p. 085015, Oct. 2019, doi: 10.1088/1361-651X/ab4b36.
- [20] F. H. Streitz, J. N. Glosli, and M. V. Patel, "Beyond Finite-Size Scaling in Solidification Simulations," *Physical Review Letters*, vol. 96, no. 22, p. 225701, June 2006, doi: 10.1103/PhysRevLett.96.225701.
- [21] J. Antonowicz *et al.*, "Structural pathways for ultrafast melting of optically excited thin polycrystalline Palladium films," *Acta Materialia*, vol. 276, p. 120043, Sept. 2024, doi: 10.1016/j.actamat.2024.120043.

- [22] S. Plimpton, "Fast Parallel Algorithms for Short-Range Molecular Dynamics," *Journal of Computational Physics*, vol. 117, no. 1, pp. 1–19, Mar. 1995, doi: 10.1006/jcph.1995.1039.
- [23] A. P. Thompson *et al.*, "LAMMPS - a flexible simulation tool for particle-based materials modeling at the atomic, meso, and continuum scales," *Computer Physics Communications*, vol. 271, p. 108171, Feb. 2022, doi: 10.1016/j.cpc.2021.108171.
- [24] D. J. Evans and B. L. Holian, "The Nose–Hoover thermostat," *The Journal of Chemical Physics*, vol. 83, no. 8, pp. 4069–4074, Oct. 1985, doi: 10.1063/1.449071.
- [25] A. Stukowski, "Visualization and analysis of atomistic simulation data with OVITO—the Open Visualization Tool," *Modelling and Simulation in Materials Science and Engineering*, vol. 18, no. 1, p. 015012, Dec. 2009, doi: 10.1088/0965-0393/18/1/015012.
- [26] P. M. Larsen, S. Schmidt, and J. Schiøtz, "Robust structural identification via polyhedral template matching," *Modelling and Simulation in Materials Science and Engineering*, vol. 24, no. 5, p. 055007, May 2016, doi: 10.1088/0965-0393/24/5/055007.
- [27] D. Khakhulin *et al.*, "Ultrafast X-ray Photochemistry at European XFEL: Capabilities of the Femtosecond X-ray Experiments (FXE) Instrument," *Applied Sciences*, vol. 10, no. 3, p. 995, Feb. 2020, doi: 10.3390/app10030995.
- [28] J. Mei and J. W. Davenport, "Molecular-dynamics study of self-diffusion in liquid transition metals," *Physical Review B*, vol. 42, no. 15, pp. 9682–9684, Nov. 1990, doi: 10.1103/PhysRevB.42.9682.
- [29] A. Bogicevic, L. B. Hansen, and B. I. Lundqvist, "Simulations of atomic structure, dynamics, and self-diffusion in liquid Au," *Physical Review E*, vol. 55, no. 5, pp. 5535–5545, May 1997, doi: 10.1103/PhysRevE.55.5535.
- [30] K. F. Kelton and A. L. Greer, *Nucleation in Condensed Matter - Applications in Materials and Biology*, vol. 15. in Pergamon Materials Series, vol. 15. Elsevier, 2010. doi: 10.1016/C2009-0-04500-0.
- [31] J. W. Arblaster, "A Re-assessment of the Thermodynamic Properties of Palladium," *Johnson Matthey Technology Review*, 2018, doi: 10.1595/205651318X696648.
- [32] C. Kittel, *Introduction to solid state physics*, 8th ed. New York, NY: John Wiley & Sons, 2004.

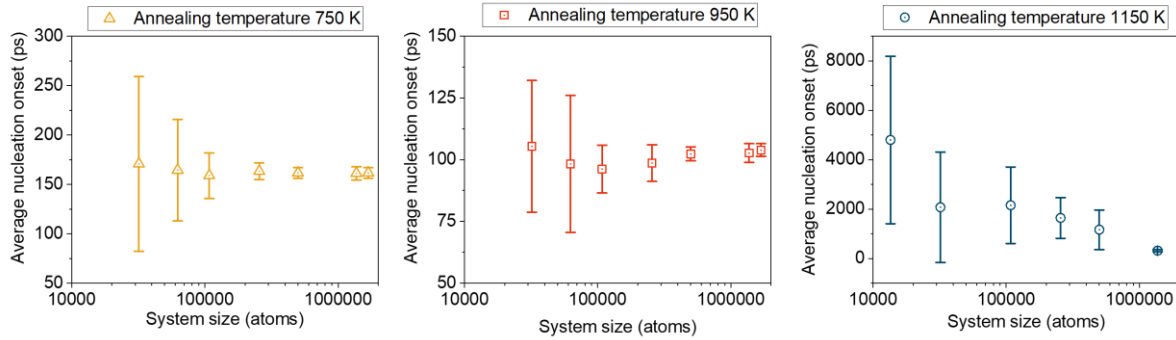
- [33] J. Q. Broughton, G. H. Gilmer, and K. A. Jackson, "Crystallization Rates of a Lennard-Jones Liquid," *Physical Review Letters*, vol. 49, no. 20, pp. 1496–1500, Nov. 1982, doi: 10.1103/PhysRevLett.49.1496.
- [34] K. Georgarakis *et al.*, "Variations in atomic structural features of a supercooled Pd–Ni–Cu–P glass forming liquid during in situ vitrification," *Acta Materialia*, vol. 59, no. 2, pp. 708–716, Jan. 2011, doi: 10.1016/j.actamat.2010.10.009.
- [35] N. Nishiyama and A. Inoue, "Supercooling investigation and critical cooling rate for glass formation in Pd–Cu–Ni–P alloy," *Acta Materialia*, vol. 47, no. 5, pp. 1487–1495, Mar. 1999, doi: 10.1016/S1359-6454(99)00030-0.
- [36] H. S. Chen and D. Turnbull, "Formation, stability and structure of palladium-silicon based alloy glasses," *Acta Metallurgica*, vol. 17, no. 8, pp. 1021–1031, Aug. 1969, doi: 10.1016/0001-6160(69)90048-0.
- [37] P. Duwez, R. H. Willens, and R. C. Crewdson, "Amorphous Phase in Palladium—Silicon Alloys," *Journal of Applied Physics*, vol. 36, no. 7, pp. 2267–2269, July 1965, doi: 10.1063/1.1714461.
- [38] O. Liubchenko *et al.*, "Ultrafast Pulsed Laser Annealing of Pd_{100-x}Si_x Thin Films," *Acta Physica Polonica A*, vol. 148, no. 4, pp. 303–303, Dec. 2025, doi: 10.12693/APhysPolA.148.303.
- [39] D. Turnbull and R. E. Cech, "Microscopic Observation of the Solidification of Small Metal Droplets," *Journal of Applied Physics*, 1950, doi: 10.1063/1.1699763.
- [40] J. Antonowicz *et al.*, "Devitrification of thin film Cu–Zr metallic glass via ultrashort pulsed laser annealing," *Journal of Alloys and Compounds*, vol. 887, p. 161437, Dec. 2021, doi: 10.1016/j.jallcom.2021.161437.
- [41] B. Lee and G. W. Lee, "A liquid-liquid transition can exist in monatomic transition metals with a positive melting slope," *Scientific Reports*, vol. 6, no. 1, p. 35564, Oct. 2016, doi: 10.1038/srep35564.
- [42] A. Meyer, "The measurement of self-diffusion coefficients in liquid metals with quasielastic neutron scattering," *EPJ Web of Conferences*, vol. 83, p. 01002, 2015, doi: 10.1051/epjconf/20158301002.
- [43] T. Iida, *The physical properties of liquid metals*. Oxford : Clarendon Press ;, 1988. Available: <http://www.loc.gov/catdir/enhancements/fy0635/86023616-d.html>, <http://www.loc.gov/catdir/enhancements/fy0635/86023616-t.html>

- [44] A. Mahata, M. A. Zaeem, and M. I. Baskes, "Understanding homogeneous nucleation in solidification of aluminum by molecular dynamics simulations," *Modelling and Simulation in Materials Science and Engineering*, vol. 26, no. 2, p. 025007, Feb. 2018, doi: 10.1088/1361-651X/aa9f36.
- [45] E. Asadi, M. Asle Zaeem, S. Nouranian, and M. I. Baskes, "Two-phase solid–liquid coexistence of Ni, Cu, and Al by molecular dynamics simulations using the modified embedded-atom method," *Acta Materialia*, vol. 86, pp. 169–181, Mar. 2015, doi: 10.1016/j.actamat.2014.12.010.
- [46] G. Wilde, J. Sebright, and J. Perepezko, "Bulk liquid undercooling and nucleation in gold," *Acta Materialia*, 2006, doi: 10.1016/j.actamat.2006.06.007.
- [47] T. Iida and R. Guthrie, "Predictions for the Sound Velocity in Various Liquid Metals at Their Melting Point Temperatures," *Metallurgical and Materials Transactions B*, vol. 40, no. 6, pp. 959–966, Dec. 2009, doi: 10.1007/s11663-009-9299-y.
- [48] Y. Ashkenazy and R. S. Averback, "Kinetic stages in the crystallization of deeply undercooled body-centered-cubic and face-centered-cubic metals," *Acta Materialia*, 2010, doi: 10.1016/j.actamat.2009.09.030.

Crystallisation kinetics of supercooled liquid palladium -Supplementary Materials

1. Preliminary test – system size

Each data point represents the mean nucleation onset time for a given annealing temperature T and system size, averaged over 10 simulation runs with distinct initial configurations. Error bars indicate the standard deviation.



2. Classical Nucleation Theory

To analyse the temperature dependence of the homogeneous nucleation rate, we employed the Classical Nucleation Theory (CNT) framework. In this section, we show how the standard CNT expression for the nucleation rate was transformed into the linear fitting form used in the present work. Firstly, we take a steady-state homogeneous nucleation rate written as:

$$J = J_0 \exp\left(-\frac{E_a}{kT}\right) \exp\left(-\frac{\Delta G^*}{kT}\right),$$

where J - nucleation rate, J_0 – a temperature-independent prefactor, E_a – activation energy associated with atomic transport, k – Boltzmann's constant, T – temperature, and ΔG^* – critical free-energy barrier for nucleation. In the present work, E_a was taken from the Arrhenius analysis shown in the main article and was therefore treated as an independently known parameter.

Within CNT, the free-energy barrier for the formation of a spherical critical nucleus is given by

$$\Delta G^* = \frac{16\pi\gamma^3}{3(\Delta G_v)^2},$$

Where γ is the solid-liquid interfacial free energy and ΔG^* is the volumetric Gibbs free-energy difference between the parent phase and nucleating phase. For solidification, ΔG^* can be approximated by the standard linearized form

$$\Delta G_v \approx \frac{\Delta H_f \Delta T}{T_m},$$

where ΔH_f is molar enthalpy of fusion, $\Delta T = (T_m - T)$ is the undercooling, T_m is the melting temperature and V_m is the molar volume. The approximation above assumes linear scaling of the thermodynamic driving force with the undercooling. Then we can substitute:

$$\Delta G^* = \frac{16\pi\gamma^3 T_m^2 V_m^2}{3\Delta H_f^2 (T_m - T)^2}$$

Then we defined a new variable $A = \frac{16\pi\gamma^3 T_m^2 V_m^2}{3k\Delta H_f^2}$, and substitute it into the nucleation rate expression:

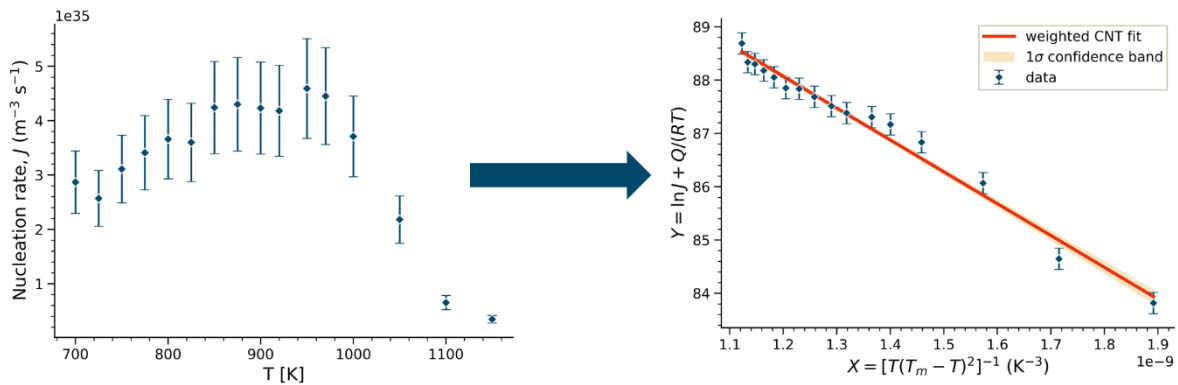
$$J = J_0 \exp\left(-\frac{E_a}{kT}\right) \exp\left(-\frac{A}{T(T_m - T)^2}\right)$$

Then we calculated the logarithm of this expression:

$$\ln J + \frac{E_a}{kT} = \ln J_0 - \frac{A}{T(T_m - T)^2}$$

In the next step, we can construct a plot where:

$$Y = \ln J + \frac{E_a}{kT} \text{ and } X = \frac{1}{T(T_m - T)^2}$$



that can be fitted by linear expression $Y = aX + b$, where $a = -A$ and $b = \ln J_0$.

The interfacial free energy is then calculated from:

$$\gamma = \sqrt[3]{\frac{3kA\Delta H_f^2}{16\pi T_m^2 V_m^2}}$$

where molar volume is given by expression:

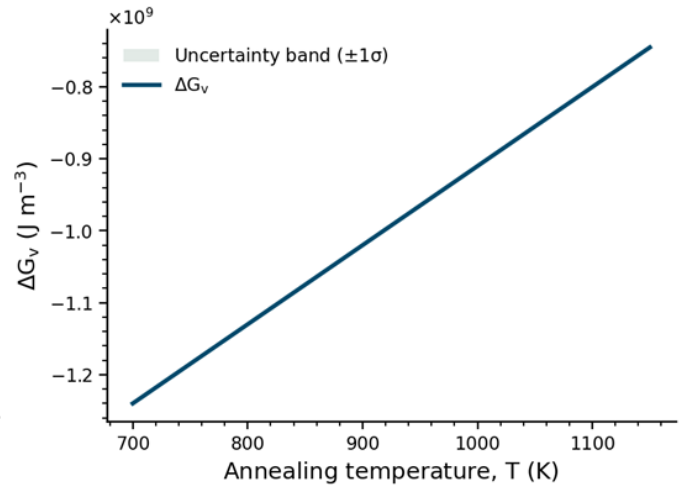
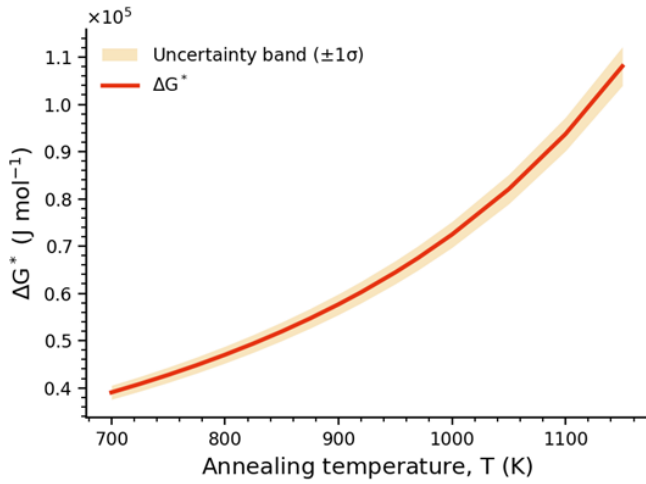
$$V_m = \frac{M}{\rho}$$

M – molar mass and ρ – mass density.

The temperature-dependent barrier, driving force, and critical radius are eventually obtained from derived expressions, yielding results:

$$J_0 = 2.31(71) \cdot 10^{41} \frac{m^3}{s}$$

$$\gamma = 0.1812(23) \frac{J}{m^2}$$



3. Temperature estimation for experimental data

